


Article

Study of Bubble Size, Void Fraction, and Mass Transport in a Bubble Column under High Amplitude Vibration

Shahrouz Mohagheghian ¹, Adam L. Still ², Brian R. Elbing ^{1,*}  and Afshin J. Ghajar ¹

¹ Mechanical and Aerospace Engineering, Oklahoma State University, Stillwater, OK 74074, USA; mohaghe@okstate.edu (S.M.); afshin.ghajar@okstate.edu (A.J.G.)

² Sandia National Laboratories, Albuquerque, NM 87123, USA; astill@sandia.gov

* Correspondence: elbing@okstate.edu; Tel.: +1-405-744-5900

Received: 16 March 2018; Accepted: 10 April 2018; Published: 17 April 2018



Abstract: Vertical vibration is known to cause bubble breakup, clustering and retardation in gas-liquid systems. In a bubble column, vibration increases the mass transfer ratio by increasing the residence time and phase interfacial area through introducing kinetic buoyancy force (Bjerknes effect) and bubble breakup. Previous studies have explored the effect of vibration frequency (f), but minimal effort has focused on the effect of amplitude (A) on mass transfer intensification. Thus, the current work experimentally examines bubble size, void fraction, and mass transfer in a bubble column under relatively high amplitude vibration ($1.5 \text{ mm} < A < 9.5 \text{ mm}$) over a frequency range of 7.5–22.5 Hz. Results of the present work were compared with past studies. The maximum stable bubble size under vibration was scaled using Hinze theory for breakage. Results of this work indicate that vibration frequency exhibits local maxima in both mass transfer and void fraction. Moreover, an optimum amplitude that is independent of vibration frequency was found for mass transfer enhancements. Finally, this work suggests physics-based models to predict void fraction and mass transfer in a vibrating bubble column.

Keywords: bubble column; vibration; bubble size; void fraction; mass transfer

1. Introduction

Bubble columns are used in many applications including aeration of organic organisms in bioreactors, indirect liquefaction of coal-slurries to produce synthetic fuels via Fischer-Tropsch process and gasification of solvent for chemical reactions. Vertical vibration is known to cause bubble clustering and retardation in gas-liquid systems [1–9]. Within a contact reactor (e.g., bubble column) these phenomena result in an increase in the mass transfer ratio due to increasing the residence time and phase interfacial area [1,2,10,11]. In addition to improved mass transfer performance, vibration decouples the bubble velocity from bubble size (retardation), offering a chance to study the hydrodynamics of bubbly flow in a more comprehensive fashion. One should note that the advantages of vibration comes at the cost of building a vibration facility as well as energy and safety expenses.

Most of the pioneering work on vibrating bubble columns was conducted between 1960 and the late 1980s [1–11]. More recently, there has been a renewed interest in the study of vibrating bubble columns [12–22]. These recent efforts have developed theoretical physics-based models to predict mass transfer and void fraction in bubble column reactor (BCR) systems undergoing vibration [18–20]. These models were tested in a limited range of data, but have yet to be fully understood or validated against a broad range of experimental data. Therefore, additional work is required to gain a fundamental understanding of the multiphase flow (including bubble size distribution, void fraction and the

resulting mass transfer) to enable scale-up and improving the operation of BCRs. The current work aims to expand the available parameter space and test current models.

In a buoyancy driven bubble column, pseudo-turbulence (bubble-induced turbulence) produces a well-mixed batch. Therefore, solving the transient mass transfer equation,

$$(1 - \varepsilon) \frac{dC}{dt} = k_L a (C^* - C) \quad (1)$$

is a common way to determine the volumetric mass transfer coefficient ($k_L a$) within a BCR [13,17,18,21–23]. Here, C is the instantaneous concentration of dissolved gas in the liquid, C^* is the saturation concentration, t is time, k_L is the liquid mass transfer coefficient, and a is the phase interfacial area. The void fraction (ε) is the ratio of the volume occupied by the gas phase to the total volume of the system. In a batch BCR this ratio is given by:

$$\varepsilon = 1 - \frac{H}{H_D} \quad (2)$$

where H is the liquid only height and H_D is the mixture height.

The bubble size distribution determines the phase interfacial area. Therefore, bubble size classification is necessary to determine an average interfacial area [24]. Use of a single length scale would be appropriate for characterizing the bubble size if the bubble shape is readily represented with a single length scale (e.g., sphere) and the shape of the size distribution was constant [24]. Sauter mean diameter (d_{32}),

$$d_{32} = \frac{\sum_{j=1}^n n_j d_j^3}{\sum_{j=1}^n n_j d_j^2} \quad (3)$$

is the most widely used characteristic length scale in bubble column studies [12,19,25,26], where n_j is the number of bubbles of size d_j . Sauter mean diameter is the ratio of the representative bubble volume to the bubble surface area, and it is frequently used when the sizes are acquired with photographic imaging. Here, the bubble cross sectional area (A_{proj}) is determined from the bubble images. Assuming ellipsoidal (or other shape) bubbles, the equivalent bubble diameter (d_{eq}),

$$d_{eq} = \sqrt{\frac{4}{\pi} A_{proj}}, \quad (4)$$

can be determined, which is the diameter of a sphere whose cross-sectional area is that of the bubble. This equivalent diameter is then used for d_j in Equation (3).

Historically, the instantaneous upward force on a bubble has been formulated by neglecting the radial motion of the bubble and surrounding liquid. The assumption of isothermal expansion and contraction justifies the application of Boyle's law to calculate the average gas volume fluctuations [2–4,18–20,27]. The validity of this approach, especially near levitation conditions is questionable given that the levitation condition exhibits strong Reynolds number dependency [4]. The interested reader is directed to Elbing et al. [28] for a more comprehensive review of previous vibrating bubble column work, but it is important to note here the work of Waghmare et al. [18] that examined void fraction and mass transfer within a pulsed bubble column. They proposed a void fraction model based on balancing the buoyancy and drag force on a single bubble. In addition, Waghmare et al. [18] used this void fraction model and the definition of mass transfer coefficient from penetration theory to propose a mass transfer model. These models were successfully tested against experimental measurements, but over a relatively narrow range. It is noteworthy that vibration makes it extremely challenging to control the test conditions due to unintended surface entrainment and resonance characteristics of the vibration facility. Furthermore, a complete body of experimental data

is not available to test the previous models. Hence, the current work will examine them over a broader range of conditions as well as propose new models.

Additionally, while most previous studies have primarily focused on frequency dependence, some have examined the influence of amplitude and found that at low power input significant improvement in column efficiency is possible with increasing amplitude [14,17]. Thus, the current work employs a multi-scale approach [29], to investigate the effect of amplitude on mass transfer with measurements of volumetric mass transfer coefficient $k_L a$, void fraction ε (column-scale) and Sauter mean diameter d_{32} (bubble-scale).

The paper is organized as follow. Section 2 presents the theory behind the proposed models for void fraction and mass transfer. Section 3 describes the experimental setup as well as instrumentations we used for our measurements. In Section 4 the results of bubble size, void fraction, and mass transfer measurement are presented. Section 4 also includes the validation of our experimental measurements and proposed models. Conclusions are given in Section 5.

2. Theory

This section presents physics-based models for the prediction of void fraction and mass transfer in a vibrating bubble column. It is noteworthy that we used subscripts L , and G for distinguishing the properties of liquid and gas phase. The transient pressure field at a particular distance (h) from the liquid free surface is

$$P = P_0 + \rho_L g h - \rho_L h A \omega^2 \sin(\omega t), \quad (5)$$

where A is the vibration amplitude, ω is the vibration angular velocity, ρ_L is the liquid density, and g is gravitational acceleration. The first term on the right hand side (P_0) is the external pressure, which is atmospheric unless pressurized. The second term represents the hydrostatic pressure, and the remaining term is the influence that the vibrations have on the pressure field $P(t)$. The transient response of the bubble radius (R) to the vibration can be formulated using the Rayleigh-Plesset equation,

$$RR'' + \frac{3}{2}R'^2 + \frac{4\nu_L R'}{R} + \frac{2\sigma}{\rho_L R} = \frac{1}{\rho_L} \left[\left(P_0 + \frac{2\sigma}{R_0} - P_v \right) \left(\frac{R_0}{R} \right)^{3\kappa} - P_0 - P(t) \right] \quad (6)$$

Here ν_L is liquid kinematic viscosity, σ is surface tension, R_0 is the reference (stationary) bubble size, P_v is the liquid vapor partial pressure inside of the bubble and κ is the gas heat capacity.

The amplitude of oscillations (r) from the bubble radius R_0 can be obtained from Equation (6) with the following assumptions:

- bubble expansion and contraction is adiabatic,
- liquid temperature is uniform and no significant thermal effect takes place,
- the bubbles contain a negligible amount of liquid vapor ($P_v \ll P_0$),
- bubble resonant frequency (f_N) is significantly larger than the vibration frequency,
- bubble radial oscillations are sinusoidal and in phase with the liquid pressure field ($R = R_0 + r \sin \omega t$),
- bubble initial/stationary radius is significantly larger than the oscillation amplitude ($R_0 \gg r$) and
- the standing acoustic wave length is much larger than the bubble radius.

In addition, order of magnitude analysis shows that the second and third terms from the left hand side of Equation (6) (corresponding to convective acceleration and viscous effects) are significantly smaller than the fluctuating pressure and transient acceleration terms. Applying these assumptions, a relationship can be formed for the scaled bubble radius oscillation amplitude under vertical vibration,

$$\frac{r}{R_0} = \frac{\rho_L A \omega^2 h}{3\kappa(P_0 + 2\sigma/R_0)} \quad (7)$$

Given the bubble size, the instantaneous upward force (buoyancy) acting on a bubble is

$$F(t) = \rho_L V(t) (g - A\omega^2 \sin(\omega t)) \quad (8)$$

Here, $F(t)$ and $V(t)$ are the instantaneous buoyancy force and bubble volume, respectively. The net upward force (i.e., time-averaged of Equation (8) over one period) is

$$\bar{F} = \rho_L V_0 g (1 - M(h)) \quad (9)$$

with

$$M(h) = \frac{1}{2\kappa} \frac{A\omega^2}{g} \frac{\rho_L A\omega^2 h}{P_0 + \frac{2\sigma}{R_0}} \quad (10)$$

Here, V_0 is the static bubble volume and $M(h)$ is the transient buoyancy (Bjerknes) number; which is the product of the scaled vibration acceleration amplitude ($A\omega^2/g$), and the scaled vibration pressure amplitude ($\rho_L A\omega^2 h / [P_0 + 2\sigma/R_0]$), and $(1/2\kappa)$. It is noteworthy that for an air-water system at thermal equilibrium ($\kappa = 1$), in the absence of significant (ambient) vacuum or micro-bubbles ($P_0 \gg 2\sigma/R_0$) the expression of $M(h)$ simplifies to the Bjerknes number (Bj),

$$Bj(h) = \frac{1}{2} \frac{\rho_L A\omega^2 h}{P_0} \frac{A\omega^2}{g} \quad (11)$$

The Bjerknes number (Bj) has been widely used in vibrating bubble column literature [3,4,6,18,19,27].

2.1. Modeling Void Fraction

Given the buoyancy force from Equation (9), an expression for the void fraction in a vibrating bubble column can be formulated. Assuming the bubbles are at terminal velocity, the buoyancy force on average must be balanced by the drag force resulting in

$$\rho_L V g (1 - M(h)) = \frac{1}{2} \rho_L U_b^2 C_D \pi R^2 \quad (12)$$

Here, C_D is the drag coefficient and U_b is the bubble rise (terminal) velocity. The relationship between the drag coefficient on a single isolated bubble ($C_{D,\infty}$) and a bubble within a swarm (C_D) [30] is

$$C_D = \frac{C_{D,\infty}}{1 - \varepsilon} \quad (13)$$

Given the definition of the superficial gas velocity $U_{SG} = Q_G/A_{CS}$, void fraction and control volume analysis shows that the bubble rise velocity (U_b) is

$$U_b = \frac{U_{SG}}{\varepsilon} \quad (14)$$

Here, Q_G is the gas volumetric flux and A_{cs} is the bubble column cross-sectional area. Combining and rearranging Equations (12)–(14) provides a relationship for the void fraction,

$$\varepsilon = U_{SG} \sqrt{\frac{C_{D,\infty}}{\frac{4}{3} d g (1 - M(h))}} \quad (15)$$

Here, d is the bubble diameter ($d = 2R$). Equation (15) is limited to low void fractions ($\varepsilon < 10\%$) since in the simplification an ε^3 term was neglected. The uncertainty in the predicted void fraction is

less than $\pm 10\%$ of the prediction. Alternatively, Hinze theory [31] can be used to predict the bubble size under vibration [18],

$$d = k \frac{\left(\frac{\sigma}{\rho_L}\right)^{\frac{3}{5}}}{P_m^{\frac{2}{5}}} \quad (16)$$

Here, k is proportionality coefficient and P_m is the time averaged input power per unit mass,

$$P_m = gU_{SG} + \frac{A^2\omega^3}{2} \quad (17)$$

The magnitude of the proportionality coefficient is dependent on the flow breakup mechanism, which for a turbulent jet (shear breakage) $k = 1.67$ based on the maximum-stable bubble size [32]. Waghmare et al. [18] determined $k = 1.70$ and thus concluded that bubble break up under vibration is due to shear force and not eddy viscosity.

The input power per unit mass is the sum of contributions from the gas injection and vibration. Note that transient vibration power is expressed by $P'_m(t) = gU_{SG} - A^2\omega^3 \sin(\omega t) \cos(\omega t)$. Equation (15) can be modified incorporating the Hinze theory-based prediction of bubble size from Equation (16) to give

$$\varepsilon = U_{SG} \sqrt{\frac{C_{D,\infty}}{\frac{4}{3}k \frac{\left(\frac{\sigma}{\rho_L}\right)^{3/5}}{P_m^{2/5}} g(1 - M(h))}} \quad (18)$$

Note that $M(H) \geq 1$ corresponds to a nonsensical scenario where bubbles experience no buoyance effect. Therefore, Equation (18) will not be in touch with the physics of the phenomenon at $M(H) \geq 1$. The average void fraction within the column can be obtained via integration through the column height,

$$\langle \varepsilon \rangle = \frac{1}{H} \int_0^H \varepsilon(h) dh = U_{SG} \sqrt{\frac{3C_{D,\infty}}{k \frac{\left(\frac{\sigma}{\rho_L}\right)^{3/5}}{\left(gU_{SG} + \frac{A^2\omega^3}{2}\right)^{2/5} g}} \left(\frac{1}{M(H)} \left(1 - \sqrt{1 - M(H)} \right) \right)} \quad (19)$$

2.2. Modeling Mass Transfer Coefficient

Employing the penetration depth theory and similar considerations from Waghmare et al. [18], the mass transfer coefficient can be expressed as

$$k_L a = \sqrt{\frac{4D_{Dif}}{t_c \pi}} \left(\frac{6\varepsilon}{d} \right) \quad (20)$$

Here, D_{Dif} is the molecular diffusion coefficient ($D_{Dif} = 2.5 \times 10^{-9}$ m/s in an air-water system) and $t_c = d/U_b$ is the contact time. Using Equations (15) and (16) the mass transfer coefficient can be expressed as

$$k_L a = 12 \sqrt{\frac{\varepsilon U_{SG} D_{Dif}}{\pi d^3}} \quad (21)$$

The average mass transfer coefficient within the column can be obtained via using the average void fraction value from Equation (19) which gives,

$$\langle k_L a \rangle = 12 \sqrt{\frac{\langle \varepsilon \rangle U_{SG} D_{Dif}}{\pi d^3}} \quad (22)$$

3. Experimental Methods

The experimental setup, schematically shown in Figure 1, was comprised of a batch bubble column mounted on a shaker table. The shaker table provided a vertical oscillation via an eccentric drive mechanism with an adjustable cam-arm linkage, which allowed the amplitude to be varied from 1–10 mm independent of vibration frequency. The shaker was powered by a three-phase, 2.2 kW (3 HP) motor (00336ES3EF56C, WEG). The frequency was controlled with variable frequency drive (ATV12HU22M2, Schneider Electric), which could be varied from 7.5 to 50 Hz. Three accelerometers were mounted directly to the shaker table to determine the vertical vibration profile as well as to quantify out-of-plane motion. The cast acrylic bubble column was 1.2 m long with a 102 mm internal diameter. It is worth mentioning that wall effects play a significant role when the column diameter is below 0.15 m [33]. Filtered (5 μm) compressed air was injected near the base of the column through a 15 gauge, 316-stainless steel round tube with an inner diameter of 1.6 mm. For more information on the effect of injector tube size on bubble size distribution in the same test facility as presented in the current work the interested reader is directed to Mohagheghian and Elbing [24]. Based on past observations [33], it is expected that the injector tube diameter has a negligible effect on gas holdup and bubble size when the injector tube diameter is larger than 1–2 mm. The injector tube had an inner diameter of 1.6 mm, which, for reference, produces an initial bubble size of 4.3 mm, when surface tension dominates detachment [34]. Thus, the dimensionless injector (sparger) opening parameter for the injector tube is 2.7 [35]. In the present work, the bubble column was filled with distilled water ($\sigma \sim 72.8 \text{ mN/m}$). All fluid heights are reported relative to the position below the static free surface ($h = 0 \text{ cm}$). The ratio of the static water height (H) to the column diameter (D) was held constant ($H/D = 8.5$) throughout testing. This aspect ratio was selected following the recommendations of Besagni et al. [36] to mitigate the effect of column height on the hydrodynamic behavior of the system. The tube was mounted vertically on the platform and sealed at both ends. The column static pressure was controlled with a pressure manifold and relief valve connected to either compressed air or a vacuum pump as needed. Pressure taps were located at 0.08 and 1.0 m liquid heights to measure the oscillating fluid pressure during vibration via a differential pressure transducer (DP15, Validyne). The differential pressure (ΔP) was used to measure the void fraction

$$\varepsilon = \frac{\Delta P}{(\rho_L - \rho_G)g\Delta H} \quad (23)$$

where ρ_G is the gas (air) density and ΔH is the vertical distance between the higher pressure tap and the pressure transducer ($\Delta H = 0.92 \text{ m}$).

A Coriolis mass flow meter (LMF 3M, Micro Motion Elite) with a range of 0.0002–0.0062 \pm 0.20% kg/min was used to measure the mass flow rate and air temperature. The flow rate was controlled using a coarse metering valve in series with a needle valve (24NS 82(A)-V8LN-SS, Parker Hannifin Corporation, Jacksonville, AL, USA) for fine adjustments. A dissolved oxygen (DO) probe (DO-BTA, Vernier Software and Technology, Beaverton, OR, USA) with a resolution of 0.007 mg/L and uncertainty of $\pm 0.2 \text{ mg/L}$ measured the DO concentration for mass transfer measurements. The DO probe was positioned three column diameters above the injector tip [22] and 0.1 diameters from the column wall [37] to account for mixing length and wall effects, respectively. Bubbles were recorded with still images (D3100, Nikon, Melville, NY, USA), high-speed (400 Hz) imaging (Phantom Miro 110, Vision Research, Wayne, NJ, USA) and video recordings (EX-F1, Casio—300 Hz; DCR-VX2000, Sony, New York, NY, USA).

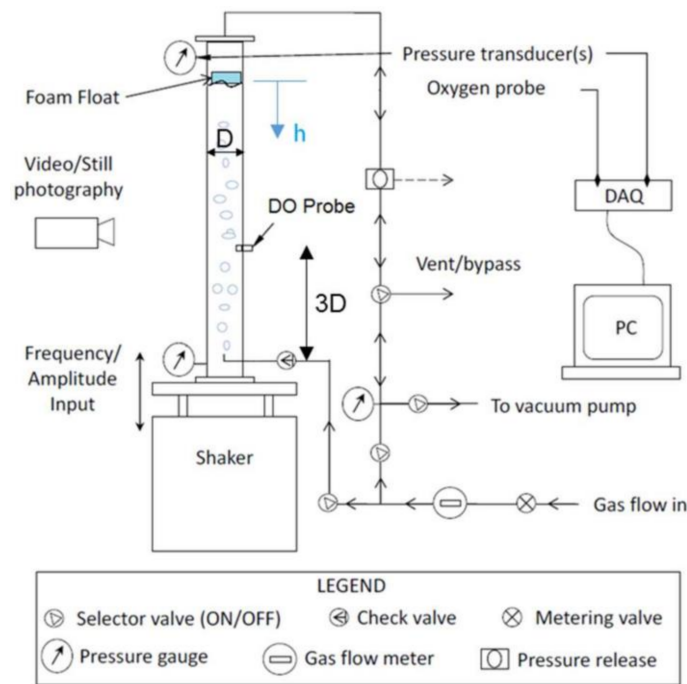


Figure 1. Schematic of the experimental setup including the bubble column mounted on the shaker table and the instrumentation.

4. Results and Discussion

Bubble size distribution, void fraction and mass transfer coefficient were measured with a liquid (distilled water) height above the injector (H) of 0.85 m. In a static column, gas holdup is virtually independent of column dimensions when the column aspect ratio is $H/D > 5$ [33]. Under vibration, Budzyński et al. [22] recommend $H > 8D$ to minimize the impact of the liquid surface deformation on void fraction measurements. Air was injected into the column at superficial gas velocities (U_{SG}) of 1.0, 2.5, 5.0, 7.5 and 10.0 mm/s. Two sets of experiments were performed at these gas flow rates. The first set was conducted to validate the experimental setup against published research data, and the second to investigate the effects of large amplitude vibration. The first set was tested at vibration frequencies of 0, 10, 12.5, 15, 17.5, 20 and 22.5 Hz with an amplitude of 1.5 or 2.5 mm, which closely matches established data in the literature [18–20]. The second set was tested at amplitudes of 4.5, 6.5 and 9.5 mm over a frequency range of 7.5–17.5 Hz, which broadens the parameter space available in the literature.

The mass transfer coefficient $k_L a$ was determined from the transient mass balance in the column. The temporal evolution of the oxygen concentration was fitted with an exponential regression to fit the form

$$\ln(C') = \frac{k_L a}{1 - \epsilon} t, \quad (24)$$

to estimate $k_L a$, where C' is the normalized instantaneous concentration,

$$C' = \frac{C^* - C(t)}{C^* - C_0}. \quad (25)$$

The gas mass flow rate (m'_G) was adjusted to the target U_{SG} and allowed to reach a steady state prior to testing. Data acquisition was initiated prior to injection to establish the initial concentration C_0 . The shaker was then started and allowed to reach steady speed. The average gas density in the column,

$$\langle \rho_G \rangle = \frac{\langle P_G \rangle}{\langle T_G \rangle R_{air}}, \quad (26)$$

is used to determine the superficial gas velocity (U_{SG})

$$\langle U_{SG} \rangle = \frac{m'_G}{\langle \rho_G \rangle A_{CS}} \quad (27)$$

Here, $\langle P_G \rangle$ is the total pressure at the middle of the column ($H = 0.425$ m), $R_{air} = 0.287$ kJ/(kg K) is the ideal gas constant; T_G , and P_G are the gas temperature and absolute pressure, respectively. Oxygen concentration was monitored and recorded until the water saturation reached ~95%, which corresponds to a time equivalent of 3τ , where

$$\tau = \frac{1}{k_L a}. \quad (28)$$

Column averaged void fraction $\langle \epsilon \rangle$ was estimated using Equation (2) with the change in the liquid-air interface height (H). The average interfacial height was determined with still images of a foam float on the air-water interface. The change in the foam float weight between the beginning and end of testing was 0.02%, which justifies that the impact of the float on the surface was constant throughout testing. A sequence of images of the column head was acquired with ImageJ (1.49v, National Institute of Health, Bethesda, MD, USA) [38–40] for each condition to determine the stagnant liquid height (H) and float during injection (H_D). The spatial calibration was determined for each image using a known reference distance in the image. Hence, each image used was individually calibrated to reduce focal length error. An average H_D was determined from the processed image data.

Sauter mean diameter (d_{32}) was measured from still images similar to other studies in the literature [18–20,24,27]. A series of images (>10) with an exposure of 250 μ s were taken at each column height ($h = 30, 45$ and 60 cm) to quantify any height dependence. The images were acquired near the mid-column cross section to reduce optical distortion from the column wall. ImageJ was used to measure the projected bubble area. A spatial calibration for each image was determined from a known reference distance in the images. The projected area measurements were then converted to an equivalent bubble diameter to calculate d_{32} (see Equations (3) and (4)). The flow visualization setup used to produce both air-water interface and bubble images is shown in Figure 2. For more information on bubble measurement uncertainty using the current experimental setup, the interested reader is directed to Mohagheghian and Elbing [24].

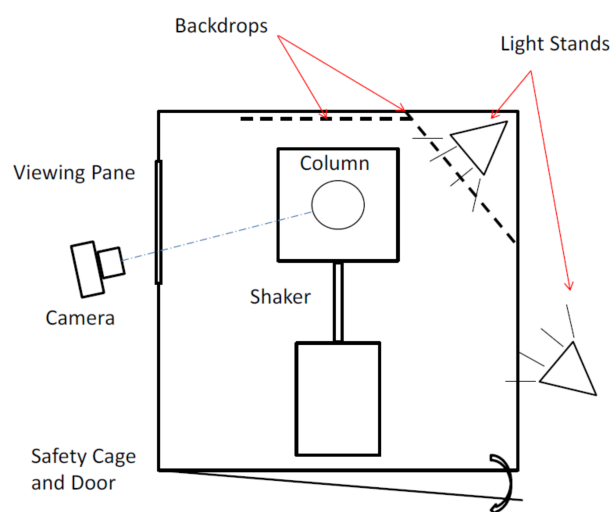


Figure 2. Schematic of camera and lighting configuration for flow visualization.

4.1. Bubble Size

Bubble imaging shows that vibration improves the interfacial area by altering the bubble size distribution from a poly-dispersed large bubble population to a more uniform distribution. It is worth mentioning that unless stated, the bubble size measurement was conducted $6D$ downstream of the injector tube to eliminate any influence from the injection condition [24]. Prior to analyzing the mean statistics, the temporal evolution of the bubble size is examined to determine steady state conditions. Figure 3 shows a time trace of d_{32} under vibration ($A = 6$ mm, $f = 10$ Hz) with $U_{SG} = 6.9$ mm/s, which shows that the bubble size becomes nearly constant after ~ 10 s. The bubble size distribution is examined in Figure 4 with a probability density function (PDF) of bubble size. For this condition, vibration modifies the bubble size distribution from a bimodal distribution (corresponding to pseudo-homogenous bubbly regime [41,42]) in static column to a unimodal distribution (corresponding to mono-dispersed homogenous bubbly regime [41,42]) due to bubble breakage. The phase-averaged results for the vibration condition can be produced by combining the known time history given the sample rate and tracking a reference point located on the column wall [43]. It is interesting that while under vibration, the shape of the distribution appears independent of phase; the largest observed bubble sizes appear to have a significant phase dependence.

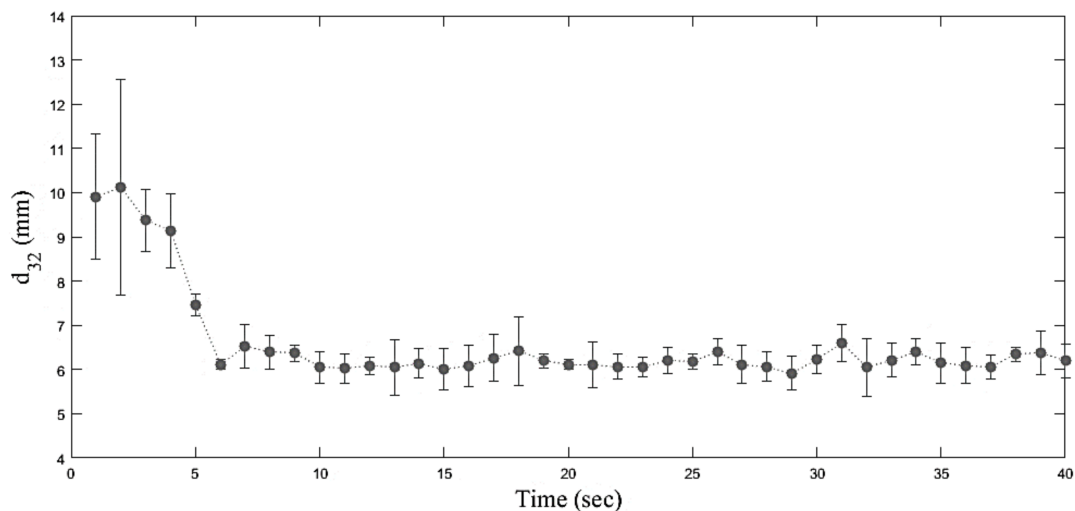


Figure 3. Temporal response of the bubble size (d_{32}) with vibration ($f = 10$ Hz, $A = 6$ mm) starting at time equals zero. ($H_0 = 85$ cm, $U_{SG} = 6.9$ mm/s, $P_0 = 1$ atm).

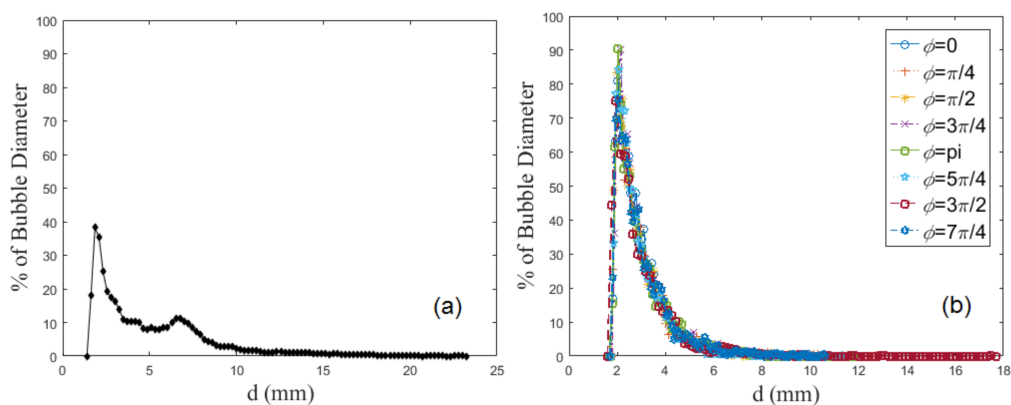


Figure 4. Probability density function of bubble sizes ($U_{SG} = 27$ mm/s, $P_0 = 1$ atm) for the (a) static column and (b) column vibrating at $f = 10$ Hz with $A = 6$ mm. Symbols for the vibration phase (ϕ) in radians is provided in the legend.

Figure 5 illustrates the bubble breakage along the column height and its dependence on the vibration amplitude. The vibration input power increases with increasing amplitude, which results in a reduction in the bubble size. Figure 5 also shows that at lower vibration amplitudes (i.e., $A = 1.5$ and 2.5 mm) the size distribution remains significantly poly-dispersed with a bimodal distribution. Another interesting finding from Figure 5 is that increasing the amplitude has a significant effect on bubble shape as well as hydrodynamic behavior of the system (operation regime). In the present work, at lower vibration amplitudes the bubble column operates at a pseudo-homogenous regime [41,42] with cap shape bubbles of various sizes (see Figure 5, $A = 1.5$ – 2.5 mm). Increasing the vibration amplitude breaks the aforementioned bubbles into smaller oblate spheroids (Figure 5, $A = 4.5$ – 9.5 mm) and shifts the operation regime from pseudo-homogenous to a mono-dispersed homogenous regime [41,42].

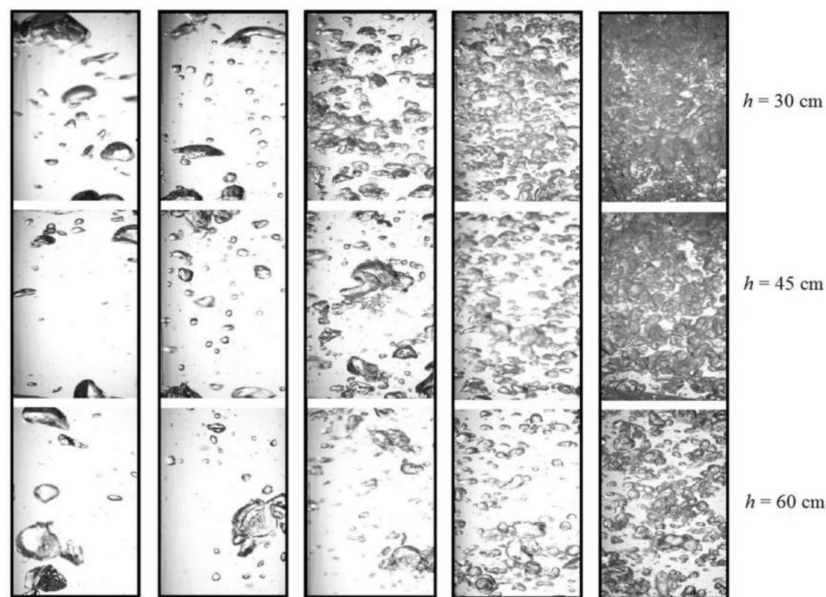


Figure 5. Instantaneous images illustrating the bubble size distribution along the column height at $f = 10$ Hz and (from left to right) $A = 1.5$ mm, 2.5 mm, 4.5 mm, 6.5 mm and 9.5 mm. ($H_0 = 85$ cm, $U_{SG} = 5.0$ mm/s, $P_0 = 1$ atm).

Unlike the static case that had a bubble size distribution partially resembling a Gaussian distribution, the vibration case is better approximated as a log-normal distribution. The bubble size scaled with the injector diameter (d_i) distributions corresponding to the conditions shown in Figure 5 are shown in Figure 6, which exhibits a log-normal distribution. These results are similar to the size distribution observed with four-point optical probes in stationary columns [44,45].

The relative change in bubble size with vibration is shown in Figure 7, which plots the change in the bubble size due to vibration ($d_{32} - d_0$) scaled by the Sauter mean diameter without vibration (d_0). These results are plotted versus the vibration amplitude (A) scaled with the injector tube diameter (d_i). Different symbols denote the test frequency, and throughout this paper, the error bars represent plus-or-minus one standard deviation. The amplitude was scaled with the injector tube diameter since under static conditions, the bubble size at detachment scales with the injector tube diameter [24]. These results show the general trend that bubble size reduction can be a significant percentage of the static condition; the general trend is increasing frequency/amplitude results in a decrease in bubble size and minimal variation in standard deviation with vibration amplitude or frequency. Simultaneous studies of the bubble size distribution (i.e., Figure 4) and Sauter mean diameter (i.e., Figure 7) under vibration suggest that a minimum bubble size limit exists ($d_{32}/d_i \approx 0.7$ & $d_{32}/d_0 \approx 0.2$) based on the fluctuating pressure field and turbulent shear balance of the surface tension. Therefore, bubbles smaller than this minimum size are extremely rare (see Figure 6).

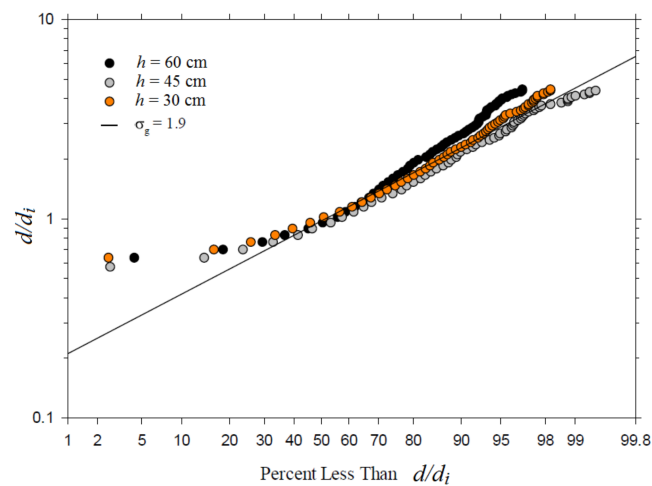


Figure 6. Distribution of the bubble diameter scaled with the injector tube diameter. Markers indicate the column height, which corresponds to locations shown in Figure 5. σ_g is the geometrical standard deviation of d/d_i . ($f = 12.5$ Hz, $A = 4.5$ mm, $U_{SG} = 5.0$ mm/s, $P_0 = 1$ atm).

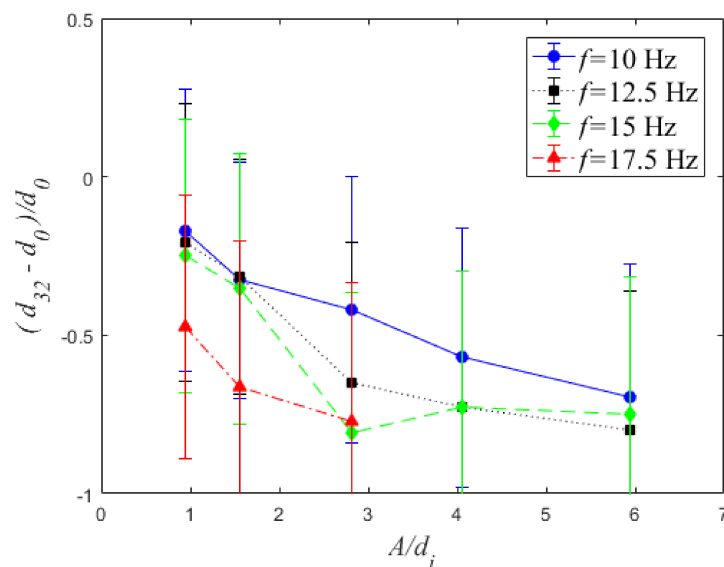


Figure 7. The change in bubble size with vibration scaled versus the Sauter mean bubble size under static conditions (d_0) plotted versus the vibration amplitude scaled with the injector tube diameter (d_i). Data was acquired at $U_{SG} = 5$ mm/s at $f = 10, 12.5, 15$ and 17.5 Hz.

It is known that bubble breakup improves mass transfer by increasing the interfacial area (a). Our results indicate that increasing the vibration amplitude (at constant frequency) produces smaller bubbles. Therefore, one could expect an increasing trend in mass transfer. However, experimental measurement of mass transfer shows a contrary result; this will be discussed in Section 4.3.

Waghmare et al. [18] proposed a correlation (Equation (16)) following the work of Hinze [31] to predict the maximum stable bubble size as a function of specific power input and the properties of the continuous phase (i.e., surface tension and density). In Equation (16) the proportionality coefficient (k) is a function of critical Weber number ($We = \rho_L U_b^2 d / \sigma$) and depends on the bubble breakup mechanism [19]. The proportionality constant has been reported as $k = 0.725$ for isotropic turbulent [31], $k = 1.67$ for shear bubble breakup [32], $k = 1.7$ for bubble breakage in a (membrane) pulsing bubble column [18,19] and $k = 1.73$ in a (piston) pulsing bubble column [46]. Waghmare et al. [18,19] used a pulsing column that produces an oscillating shear flow from use of a membrane, which could

explain the reported proportionality constant closely matching that of the shear breakup. The fit of Waghmare et al. [18,19] is compared with the current vibrating column results in Figure 8. Vibrating the whole column produces an oscillatory pressure field with negligible shear, which is distinctly different from the shear breakup mechanisms. The current results in Figure 8 demonstrate a minimum input power ($P_m \sim 0.54$ W/kg) to reduce the bubble size, and below this threshold the bubble diameter remains nearly constant nominally at the static bubble column value. Once the threshold is exceeded, there is a decrease in bubble size with increasing input power consistent with Equation (16) when $k = 3.4$. Note that close to the threshold level there is evidence that the vibration produces a slight increase in bubble size relative to the static case (d_0), which is consistent with data from Waghmare et al. [18,19].

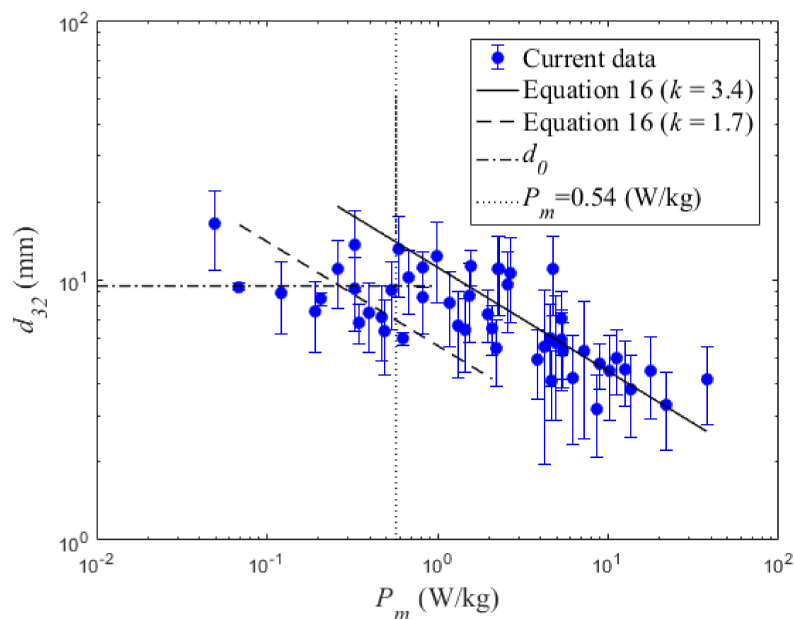


Figure 8. The bubble Sauter mean diameter (d_{32}) plotted versus the input power, Equation (17). These results are compared against Hinze based correlations for the maximum stable bubble size as well as the static bubble column Sauter mean diameter (d_0).

4.2. Void Fraction

Void fraction was measured at $A = 1.5$ and 2.5 mm over a range of frequencies (0–22.5 Hz) and superficial gas velocities (1.0–10.0 mm/s). The current void fraction measurements (ϵ) at $U_{SG} = 2.5$ mm/s and $A = 2.5$ mm are presented in Figure 9 scaled with the static column void fraction (ϵ_0). Error bars in Figure 9 represent the standard deviation of surface displacement fluctuations. These conditions were selected since they closely match that of Waghmare et al. [18] ($A = 2.46$ mm, $U_{SG} = 2.5$ mm/s), which are included for comparison. There is excellent agreement between the current results and those of Waghmare et al. [18]. These results also demonstrate a near step change in void fraction close to $f = 17.5$ Hz and the chaotic oscillations at the free surface at these high frequencies (i.e., large error bars when $f > 15$ Hz).

A wider range of test conditions are shown in Figure 10 with the void fraction (ϵ) scaled with static column void fraction (ϵ_0) and plotted versus the vibration amplitude scaled with the injection tube diameter (d_i). These results were acquired at a single injection condition, $U_{SG} = 5$ mm/s. The general trend is that increasing amplitude and/or frequency results in an increase in void fraction. Furthermore, the step change can be observed at each amplitude tested with the required frequency decreasing with increasing amplitude. These observations suggest that the void fraction should be proportional to

a product of the frequency and amplitude, such as power input per unit mass (P_m) or the transient buoyancy number ($M(H)$).

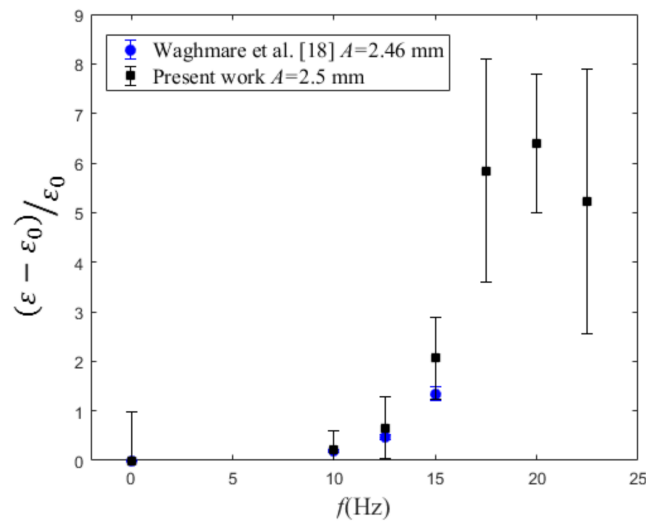


Figure 9. The void fraction (ε) scaled with the static column void fraction (ε_0) plotted versus the vibration frequency ($U_{SG} = 2.5$ mm/s). The current results are compared with that of Waghmare et al. [18].

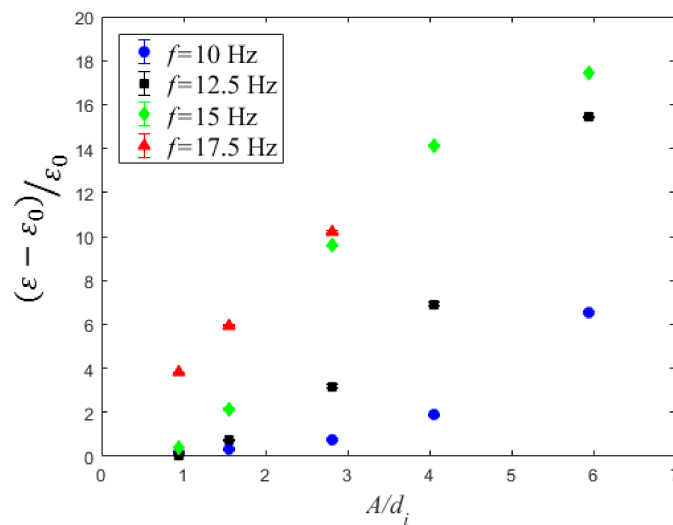


Figure 10. The void fraction (ε) scaled with the static column void fraction (ε_0) plotted versus vibration amplitude (A) scaled with the injector tube diameter (d_i). All data was collected at $U_{SG} = 5$ mm/s.

The current void fraction results are plotted versus $M(H)$ and P_m in Figure 11 as well as a power-law fit for each plot. These results are consistent with Waghmare et al. [18]. Also, Figure 11 demonstrates that the void fraction is dependent on both of these parameters; however, it shows a stronger dependency on $M(H)$. The correlation between $\varepsilon/\varepsilon_0$ and $M(H)$ supports the theory in Equation (15) that $M(H)$ is a primary factor in scaling the void fraction.

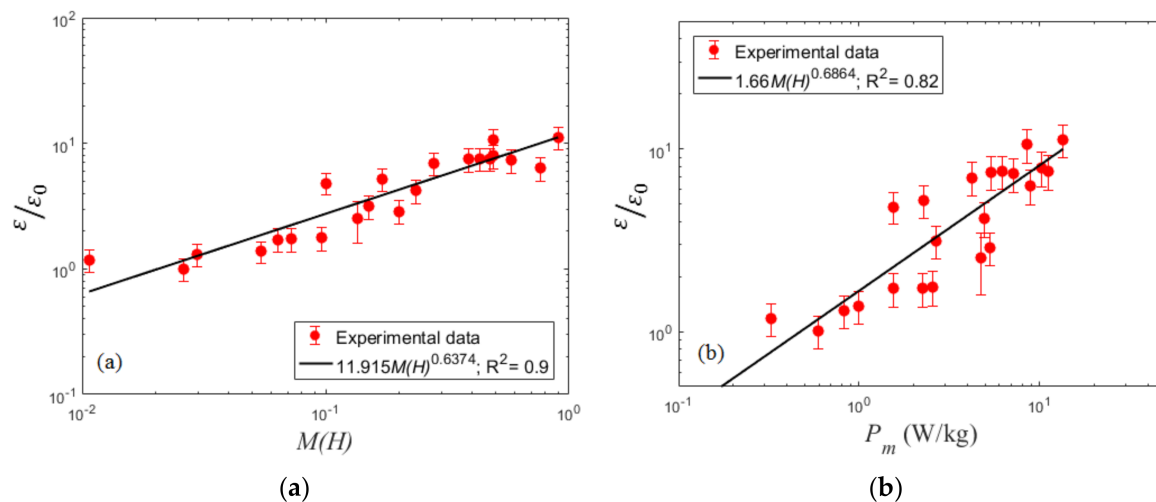


Figure 11. (a) void fraction versus $M(H)$; (b) void fraction versus the specific power input (P_m).

The current void fraction results are compared with the predictive models proposed in the current work as well as Waghmare et al. [18] in Figure 12. Detailed investigations revealed that water is a low Morton number liquid ($Mo = g\mu_L^4/\rho_L\sigma^3 \sim 2.6 \times 10^{-10}$) [47]. Low Morton number liquids are characterized by a minimum in $C_{D,\infty}$ vs. Re (Reynolds number) trend. Bubble Reynolds number ($Re = U_b d/\nu_L$; is based on bubble size (d), rise velocity and, kinematic viscosity of the liquid (ν_L)) in this work ranges from 125 to 7000. Within the aforementioned range of Reynolds number and system properties ($Mo \sim 2.6 \times 10^{-10}$) the drag coefficient exhibits a minimum ($C_{D,\infty} = 0.15$) at $Re = 440$ and levels off when $Re > 4000$ ($C_{D,\infty} = 2.74$). Therefore, using a proper Reynolds number based correlations to predict the drag coefficient is vital to produce an accurate model to predict void fraction. In the present work, experimental measurements of $C_{D,\infty}$ from Brennen [48] were used instead of using a correlation to calculate the drag coefficient on a single bubble. Figure 12 illustrates the predictions of $\varepsilon/\varepsilon_0$ from this work as well as that of Waghmare et al. [18] in comparison with experimental measurements at various $M(H)$'s. Figure 12 shows that Equation 19 has no success predicting the $\varepsilon/\varepsilon_0$ accurately.

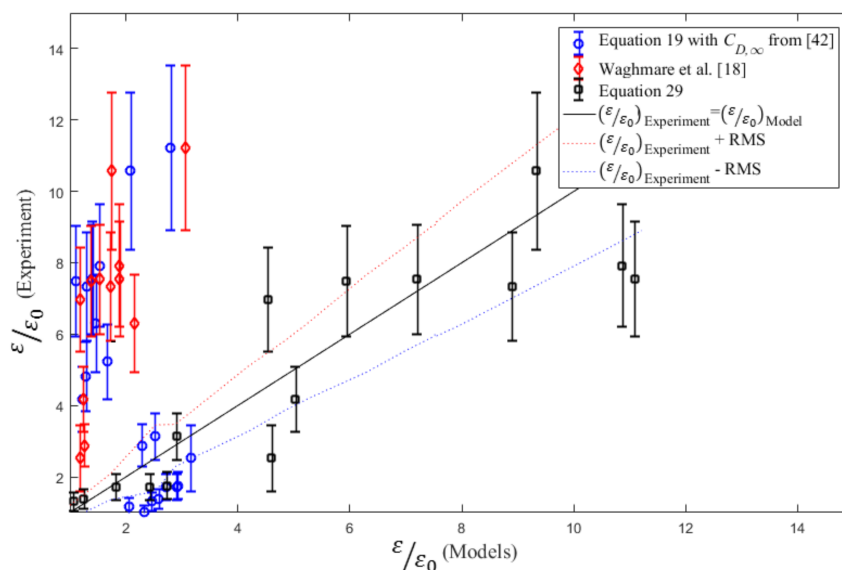


Figure 12. Comparison of the experimental data the predicted void fraction by models from this work and Waghmare et al. [18]. RMS is the root mean square of $\varepsilon/\varepsilon_0$.

We used a trial and error approach to find a model that scales the void fraction over the entire test range of $M(H)$. Starting with Equation (12) with $C_{D,\infty} = 24/Re$ a model for the void fraction is produced,

$$\langle \varepsilon \rangle = K_\varepsilon \frac{36U_{SG}v_L}{g} \left[\frac{\left(gU_{SG} + \frac{A^2\omega^3}{2} \right)^{\frac{2}{5}}}{k \left(\frac{\sigma}{\rho_L} \right)^{\frac{3}{5}}} \right]^2 \left[\frac{1}{M(H)} \ln \left(\frac{1}{1 - M(H)} \right) \right]. \quad (29)$$

K_ε is assumed to be a constant related to experimental setup (here $K_\varepsilon = 50$). Figure 12 shows that Equation (29) offers an acceptable physics base prediction of $\varepsilon/\varepsilon_0$ within the tested range. It is noteworthy that Equation (29) is only valid within the tested range and any predictions beyond the current parameter space must be verified against experimental data.

Example images from the recording of the free surface are shown in Figure 13. Examination of these images reveals that the onset of air entrainment at the free surface occurs nominally at $M(H) \sim 0.3$. The chaotic oscillation of the liquid free surface captures large pockets of air, this phenomenon introduces an artificial increase in the measured void fraction. Surface entrainment is due to surface disintegration and free surface over turn at the wall [49]. Surface disintegration happens at a wavy free surface when the wave crest evolves into a narrow-bottled neck fountain, which ultimately breaks into drop(s). Hashimoto and Sudo [50] argued that the column aspect ratio (H/D) and vibration amplitude set the onset of surface disintegration. Air bubbles enter the column at the surface due to impact of the disintegrated drops. Note that on one hand increasing the vibration frequency reduces the size of the disintegrated drops [51]. On the other hand, size of entrained air bubbles are proportional to the size of the drops and the wavelength of surface waves [51]. Over turn of the wave crests at the column wall produces a thin film at the wall that also captures air bubbles into the column.

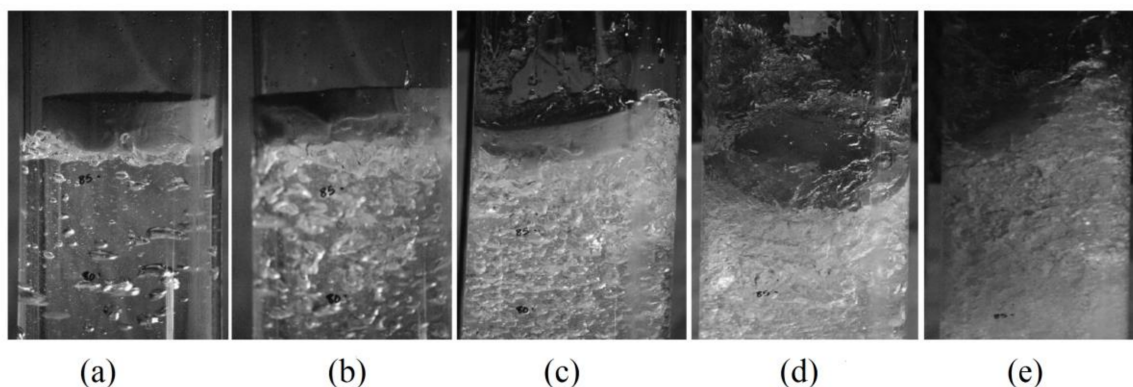


Figure 13. Air-Water interface at $f = 12.5$ Hz, $H_0 = 85$ cm and (from left to right) (a) $A = 1.5$ mm ($M(H) = 0.035$), (b) 2.5 mm ($M(H) = 0.098$), (c) 4.5 mm ($M(H) = 0.317$), (d) 6.5 mm ($M(H) = 0.661$) and (e) 9.5 mm ($M(H) = 1.41$).

Surface entrainment elevates the free surface and increases the measured void fraction. One could now see the reason why models without considering the effect of surface entrainment will fail at predicting the void fraction.

4.3. Volumetric Mass Transfer Coefficient

Particular frequencies and vibration modes correspond to significant intensification of mass transfer and void fraction [12–22]. The current mass transfer measurements were validated with comparison to a subset of conditions tested in Waghmare et al. [19]. Results from both studies are provided in Figure 14 with the volumetric mass transfer coefficient ($k_L a$) plotted versus the vibration frequency for a single injection rate ($U_{SG} = 2.5$ mm/s) and vibration amplitude ($A = 2.5$ mm). While the two results partially differ in the magnitude (with worth case of 35% difference at 20 Hz), overall

they are consistent in trend as well as location of excitation modes ($f = 17.5$ Hz). Both results show a steady increase in the mass transfer coefficient from ~ 10 Hz to 17.5 Hz, and at 20 Hz a slight drop creates a local maximum. It is noteworthy that at $f = 20$ Hz a repeatable response of the setup was observed that could correspond to the natural frequency of the shaker table. Detailed investigations in the vicinity of $f = 20$ Hz showed that $k_L a$ at $f = 19$ Hz and $f = 21$ Hz lies within the uncertainty range of Waghmare et al. [19]. The decay mechanism at $f = 20$ Hz was not investigated here; however, one can see the same behavior in data from Waghmare et al. [19] as well. From Figure 14 one could draw a conclusion that vibration modes corresponding to mass transfer intensification are independent of vibration method since both piston pulsing from Waghmare et al. [18,19] and column shaking in the present work produced almost identical results. However, more comprehensive data would be needed for both vibration methods to fully understand the difference and the impact of the vibration methods on $k_L a$ and void fraction results. Note that chaotic surface disintegration at higher frequencies causes larger error bars on the present data in Figure 14 due to unintended surface entrainment (see Figure 9). Table 1 summarizes the measurements of $k_L a/k_L a_0$ in the current work; here, $k_L a_0$ is the volumetric mass transfer coefficient in a static column. As expected increasing the vibration amplitude increases the $k_L a$; however, $A = 2.5$ mm and $f = 17.5$ Hz corresponds to an agitation mode at which the $k_L a$ trend exhibits a significant peak. Bubble size is smaller at $A = 2.5$ mm and $f = 20$ Hz, the peak in $k_L a$ at $A = 2.5$ mm and $f = 17.5$ Hz shows that the phase interfacial area is not the only contributing factor in improving the mass transfer. In other words, although d_{32} continues to decrease in Figure 7, $k_L a/k_L a_0$ exhibits an optimum at $A/d_i = 4.25$ (Figure 15). Additionally, $(\varepsilon - \varepsilon_0)/\varepsilon_0$ exhibits a larger increase and does not show a reduction after $A/d_i > 4.25$ (see Figure 10) comparing with $(k_L a - k_L a_0)/k_L a_0$. This steady rise of void fraction agrees with a steady reduction in bubble size (see Figure 7). However, the presence of a diminishing $(k_L a - k_L a_0)/k_L a_0$ values for $A/d_i > 4.25$ (Figure 15) indicates that improving $k_L a$ is not simply due to increased specific interfacial area (a), but rather an improvement in liquid mass transfer coefficient (k_L) dependent upon the frequency/amplitude combinations leading to a tuned column. This independent effect of frequency on k_L has been reported in [1].

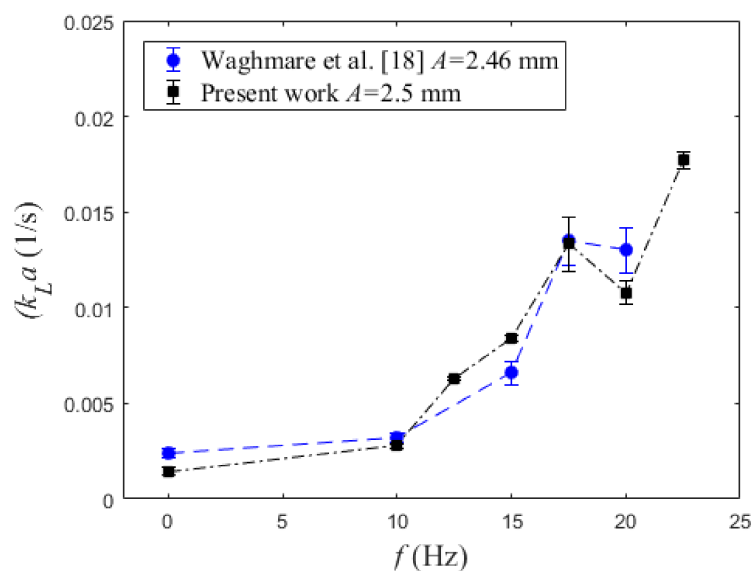


Figure 14. Comparison of $k_L a$ versus f with data from Waghmare et al. [18], $U_{SG} = 2.5$ mm/s.

The maxima in Figure 15 suggest that within the tested frequency range an optimum amplitude exists. Even with the suggestion of an optimum amplitude, nearly equivalent mass transfer coefficients can be found at other frequency/amplitude combinations. An example is presented to illustrate the necessity to optimize the frequency/amplitude combination for $k_L a$. Both $f = 12.5$ Hz, $A = 4.5$ mm and $f = 22.5$ Hz, $A = 2.5$ mm produce nearly equivalent $k_L a$, which represents an 80% increase in amplitude

traded for a 44% reduction in frequency. This trade gives a 44% reduction of vibration power P_m , where P_m is the specific input vibration power taken as the mass specific integral of force times the velocity over a quarter period,

$$P_m = \frac{A^2 \omega^3}{2} \quad (30)$$

Ultimately, this example serves to emphasize the need for a model that includes unifying parameters composed of frequency/amplitude combinations that can predict and optimize mass transfer in a vibrating bubble column.

Table 1. Normalized volumetric mass transfer $k_L a/k_L a_0$ ($U_{SG} = 5.0$ mm/s).

f (Hz)	$A = 1.5$ mm	$A = 2.5$ mm	$A = 4.5$ mm	$A = 6.5$ mm	$A = 9.5$ mm
7.5	-	-	-	2.7	4
10	1.5	2	2.6	2.9	2.3
12.5	2.1	2.7	6.6	6.8	6.9
15	2.5	5.5	5.8	10.2	6
17.5	2.9	7.6	8.3	-	-
20	4.4	6.2	-	-	-
22.5	-	7	-	-	-

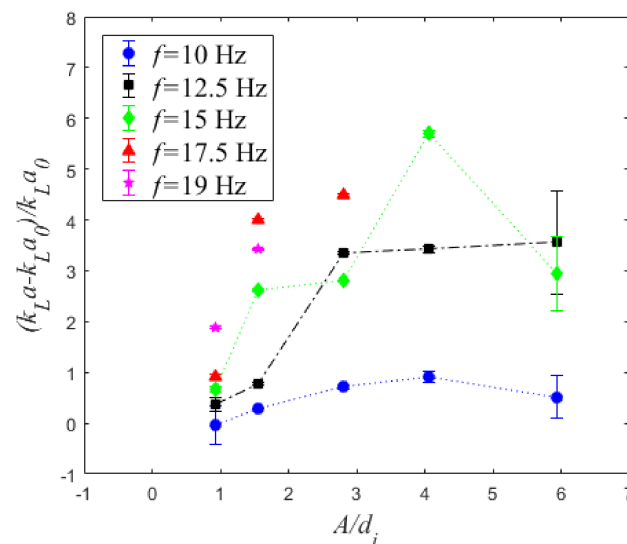


Figure 15. Non-dimensional mass transfer coefficient versus non-dimensional vibration amplitude for $f = 10, 12.5$ and 15 Hz ($U_{SG} = 5.0$ mm/s).

Figure 16 demonstrates the dependence of $k_L a/k_L a_0$ on $M(H)$ and P_m as well as a logarithmic fit. Given the importance of both power input (P_m) and transient buoyancy number ($M(H)$) in governing the physical behavior of the system, Figure 16 shows that $k_L a/k_L a_0$ exhibits a stronger dependency on $M(H)$ in comparison with P_m .

Figure 17 illustrates the predictions of $k_L a/k_L a_0$ from this work as well as that of Waghmare et al. [18] in comparison with experimental measurements at various $M(H)$'s. We used the same approach as Waghmare et al. [18] to build a correlation to predict mass transfer using a better estimation of void fraction. When $M(H) < 0.3$ both models predict the volumetric mass transfer coefficient relatively well; however, onset of surface entrainment attributes to the model failure. Due to scarcity of models for prediction of mass transfer in vibrating bubble columns, we decided to provide a correlation to predict mass transfer and test it within the range of our experimental data as well as that of Waghmare et al. [18].

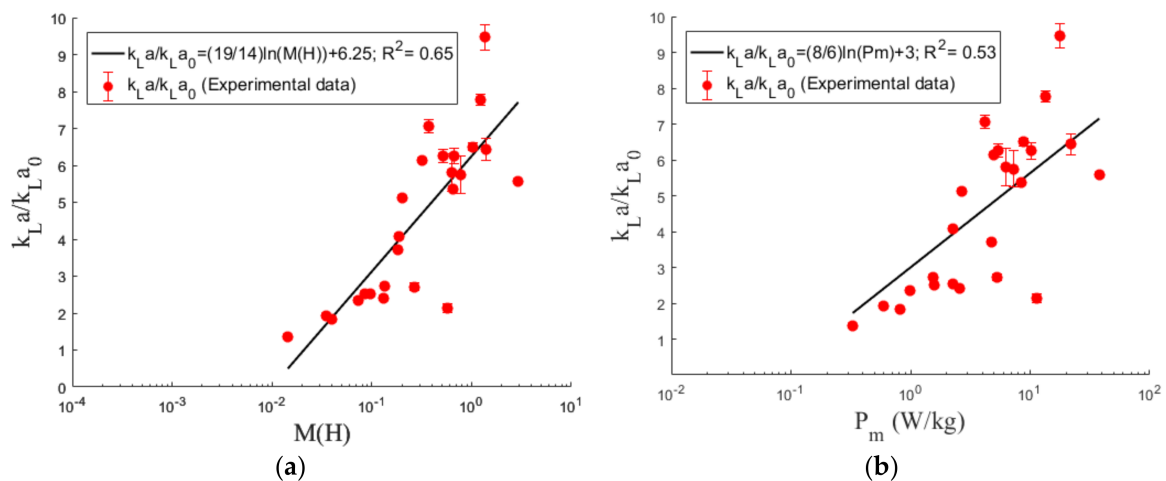


Figure 16. (a) $k_L a$ versus $M(H)$; (b) $k_L a$ versus the specific power input (P_m).

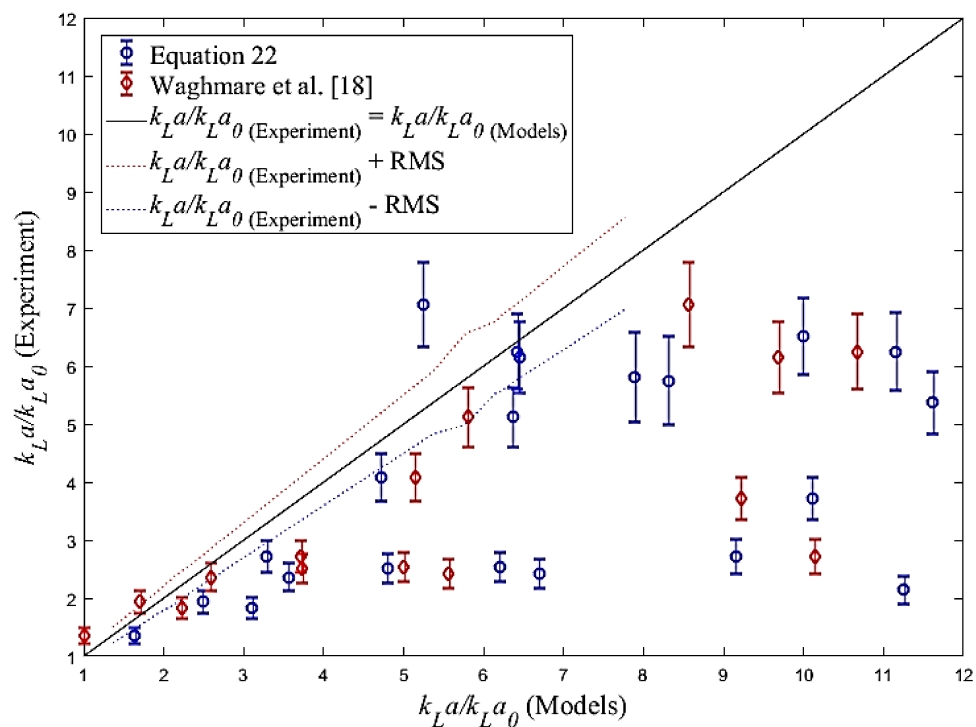


Figure 17. Comparison of the experimental data with the predicted $k_L a/k_L a_0$ by models from this work and Waghmare et al. [18]. RMS is the root mean square of $k_L a/k_L a_0$.

Previous works [10,16–19] have contributed a physics-based model that supports the theory that specific power P_m and superficial gas velocity U_{SG} are the primary factors in mass transfer. However, Waghmare et al. [18,19] have been supported in part by limited experimental evidence. The model is given by the expression:

$$k_L a \propto P_m^{0.8} U_{SG} \quad (31)$$

Regression of the data from the present research shows that $M(H)$ is a stronger factor than P_m . It is noteworthy that B_j was selected for regression instead of M due to the fractional difference between B_j and M and repeated use of B_j in vibrating bubble column literature. Upon further investigation, data from Waghmare et al. [19] also show the same result. A simple hypothesis test (t -test) on the exponents of the P_m terms compared to the theoretical exponential value of 0.8 found in Equation (31)

indicates that none of the regression results using data from Waghmare et al. [19] are statistically equal to the exponent; see Figure 18. Taken together with the U_{SG} data, as in Equation (32), regression of the data gives:

$$k_L a \propto P_m^{0.56} U_{SG}^{0.87} \quad (32)$$

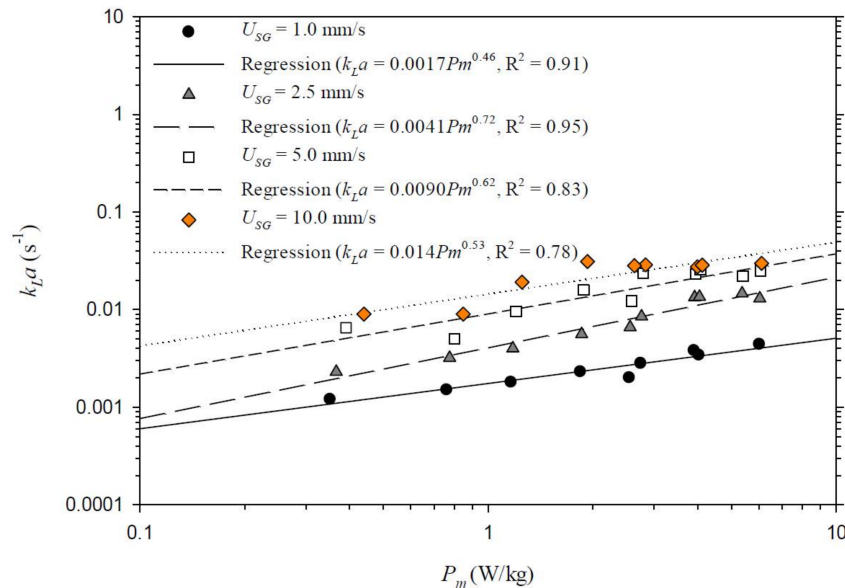


Figure 18. Regression results of Waghmare et al. [19] for $U_{SG} = 1.0$ to 10.0 mm/s.

Using Minitab, linear regressions and ANOVA analyses were performed on both data from Waghmare et al. [19] and the present research. Void fraction and volumetric mass transfer coefficient models from Waghmare et al. [19] are given in Equations (33) and (34), here, U_{SG} , P_m and Bj can be analyzed separately for independent influences on mass transfer coefficient. Assuming U_{SG} has a linear contribution to the results P_m and Bj can be analyzed independently. Analysis over the present work and that of Waghmare et al. [19] shows Bj scales the $k_L a$ more prominently in comparison with P_m (see Figure 19). Independent linear regression of both data sets as a function of Bj gives exponential values that are statistically equivalent. Therefore, P_m may not be as significant a factor as initially proposed.

$$\varepsilon = 2.25 \left[\frac{U_{SG} P_m^{0.4}}{\left(\frac{\sigma}{\rho_L}\right)^{0.6} \left(\frac{g}{\sqrt{v}}\right)^{2/3}} \right] E(Bj) \quad (33)$$

$$E(Bj) = \frac{3}{Bj} \left[1 - (1 - Bj)^{1/3} \right]$$

$$k_L a = 4.58 \left[\frac{U_{SG} \sqrt{D} P_m^{0.8}}{\left(\frac{\sigma}{\rho_L}\right)^{1.2} \left(\frac{g}{\sqrt{v}}\right)^{1/3}} \right] E(Bj) \quad (34)$$

$$E(Bj) = \frac{3}{2} \left[\frac{1 - (1 - Bj)^{2/3}}{Bj} \right]$$

A linear ANOVA analysis over U_{SG} , P_m and Bj showed that Bj is the prominent term in scaling the mass transfer, and results of the present work as well as those from Waghmare et al. [19] are in agreement with correlation of Equation (33) as shown in Figure 20,

$$k_L a = K P_m^{-0.46} U_{SG}^{0.91} B_j^{0.74} \quad (35)$$

e, K is a constant term related to the experimental conditions and fluid properties, here, $K = 0.015$.

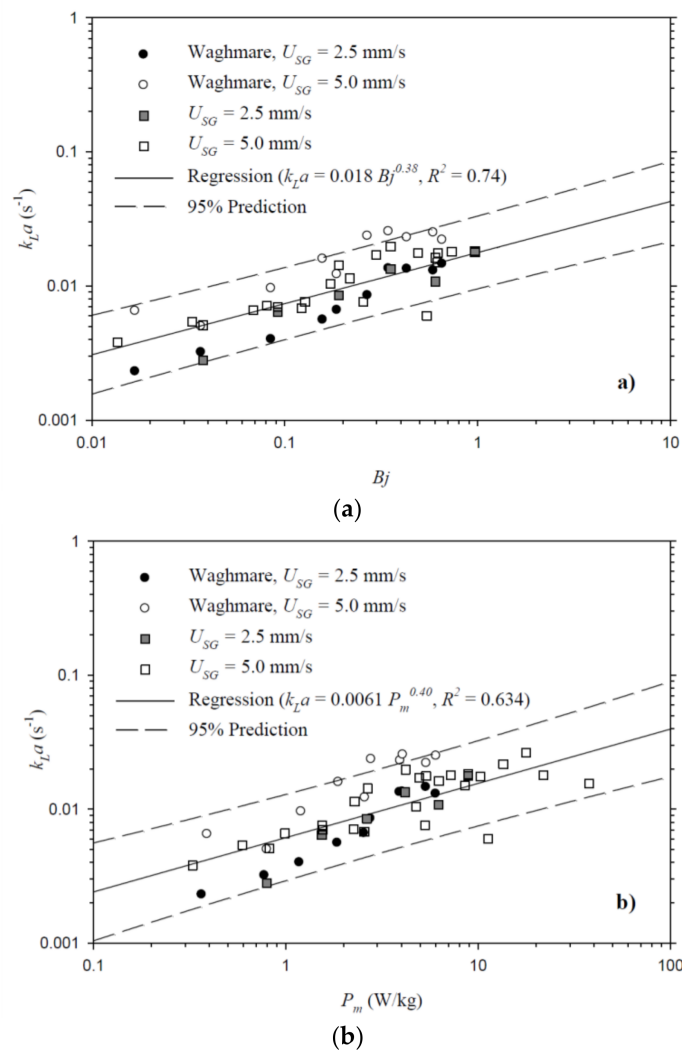


Figure 19. Effect of (a) Bj and (b) P_m on $k_L a$ over present work and that of Waghmare et al. [19].

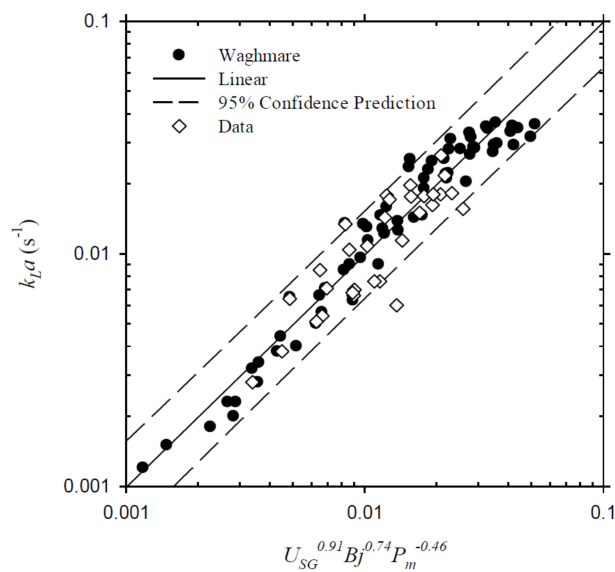


Figure 20. Regression Correlation of Waghmare et al. [19] data and results of the present research.

5. Conclusions

Bubble size, void fraction and mass transfer were investigated in a vibrating bubble column setup over the amplitude range of 1.5–9.5 mm at frequency ranges of 7.5–22.5 Hz. The vibration conditions at higher amplitudes had not been tested previously and experiments were performed to determine if separate influences exist on d_{32} , ε and $k_L a$. Vibration conditions in the present work correspond to the Bjercknes number range of $0 \leq M(H) < 1$. The results indicate special cases do exist for mass transfer improvement at reduced power requirements. Frequency maxima (agitation modes) were observed similarly for both high and low amplitudes in the frequency range tested as noted in the literature. An optimum amplitude ($A/d_i = 4.25$) was observed to exist for $k_L a$ intensification, but not for void fraction.

To study the effect of vibration on bubble size, measurements were conducted at three column heights. Expectedly increasing the vibration frequency and amplitude decreased the Sauter mean diameter (d_{32}). At higher amplitudes d_{32} decayed to a minimum at lower frequencies. The measured d_{32} was successfully tested against Hinze [30] correlation. The proportionality coefficient in the present work ($k = 3.4$) is different from those reported in shear bubble breakage and pulsing column literature ($k = 1.67$ and 1.7 respectively). The current k attributes to the difference in the physics of bubble breakup in the present work (shaking-column) and those reported in the literature (pulsing-column). The PDF of bubble size under vibration exhibits a constant shape at different phases; however, vibration phase modifies the right leg of the distribution and consequently the d_{32} . The smallest bubble sizes ($d_{32} \sim 2$ mm) were obtained at high frequency/amplitude combinations, and size distributions were found to be log-normal. Direct measurement techniques confirm the log-normal (bubble size) distribution. Bubble size shows a consistent decreasing trend with increasing the vibration amplitude while mass transfer intensification decreased for larger amplitudes ($A > 6.5$ mm). Therefore, the data suggests it is not simply increasing interfacial surface area, a , which increases the product $k_L a$, but rather the excitation modes established by specific frequency/amplitude combinations increase k_L by enhancing the diffusion mechanism.

Void fraction was measured via free surface displacement and differential pressure measurement along the column. Void fraction data in the present work shows strong dependency on $M(H)$. A physics-based model was proposed to predict the void fraction under vibration by using the reported experimental data of the drag coefficient on a rising bubble. Results show that the current model presents an improved prediction of void fraction; however, at the onset of surface entrainment the current model is not able to provide an accurate prediction of void fraction. A correlation was presented to predict the void fraction with acceptable accuracy within the tested range.

A physics-based model was proposed for mass transfer prediction; the current model was partially successful in predicting the volumetric mass transfer coefficient; however, it fails at the onset of surface entrainment. The mass transfer and void fraction data were analyzed using regression and linear ANOVA methods to determine a unifying parameter for the purpose of scaling $k_L a$. Results of this research show that mass transfer as well as void fraction can be scaled using the Bj , U_{SG} and P_m . The proposed correlation was successfully tested against present data and those of Waghmare et al. [18,19].

Based on the results in this work, a main branch of future work is advised. Surface disintegration due to chaotic vibration at high amplitudes causes large batches of air to enter the liquid phase and as a result artificially increase the average void fraction. Characterization of surface entrainment from vibration is vital to any physical-based model that predicts the void fraction and mass transfer and future work on this part of the vibrating bubble column scale up is advised.

Acknowledgments: The authors would like to thank Dr. Swanand Baghwat and Luke Walker for their assistance with this work. This work was funded in part by Sandia National Laboratories, Albuquerque, NM. Sandia National Laboratories is a multimission laboratory managed and operated by National Technology & Engineering Solutions of Sandia, LLC, a wholly owned subsidiary of Honeywell International Inc., for the U.S. Department of Energy's,

National Nuclear Security Administration under contract DE-NA0003525. The views expressed in the article do not necessarily represent the views of the U.S. Department of Energy or the United States Government.

Author Contributions: Adam L. Still and Afshin J. Ghajar conceived and designed the experiments. Adam L. Still performed the majority of experiments and Shahrouz Mohagheghian performed additional experiments. Brian R. Elbing as well as other authors contributed to the data analysis and writing of the paper.

Conflicts of Interest: The authors declare no conflict of interest.

Abbreviations

Nomenclature

A	Vibration Amplitude (mm)
A_{SC}	Column Cross Section Area (mm^2)
A_{proj}	Projected Two-Dimensional Area (mm^2)
a	Interfacial Surface Area (mm^2)
Bj	Bjerknes Number from Previous works [18–20,27]
C	Dissolved Gas Concentration (mg L^{-1})
C_0	Initial Dissolved Gas Concentration (mg L^{-1})
C^*	Dissolved Gas Concentration at Saturation or Equilibrium (mg L^{-1})
C'	Normalized Instantaneous Gas Concentration
C_D	Coefficient of Drag for a Bubble Swarm
$C_{D,\infty}$	Coefficient of Drag for a Single Isolated Bubble
D	Column Diameter (mm)
D_{Dif}	Molecular Diffusion Coefficient ($\text{mm}^2 \text{s}^{-1}$)
d	Bubble Diameter (mm)
d_{eq}	Area Equivalent Bubble Diameter (mm)
d_i	Injector Tube Diameter (mm)
d_0	Sauter Mean diameter in static column (mm)
d_{32}	Sauter Mean Diameter (mm)
F	Buoyancy Force (N)
f	Vibration Frequency (Hz)
f_N	Bubble Resonance Frequency (Hz)
g	Gravitational Acceleration (m s^{-2})
H_D	Dynamic Gas-Liquid Interface Height (m)
H	Static Liquid Height (m)
ΔH	Vertical Distance between Pressure Taps (m)
h	Liquid Height Above the Point of Interest (m)
K	Proportionality Coefficient in $k_L a$ Correlation
K_ϵ	Proportionality Coefficient in ϵ Correlation
k	Proportionality Coefficient in Hinze Correlation
k_L	Liquid Mass Transfer Coefficient (m/s)
$k_L a$	Volumetric Mass Transfer Coefficient (s^{-1})
$k_L a_0$	Volumetric Mass Transfer Coefficient in static column (s^{-1})
$M(H)$	Transient Buoyancy (Bjerknes) Number
Mo	Morton Number
m'_G	Mass Flow Rate of Gas (kg s^{-1})
n	Number Count
P_G	Gas Phase pressure at Injection Manifold (Pa)
P_m	Vibration Specific Power ($\text{m}^2 \text{s}^{-3}$)
$P_m'(t)$	Transient Vibration Specific Power ($\text{m}^2 \text{s}^{-3}$)
P_o	Liquid Vapor Pressure (Pa)
P_0	External or Ambient Pressure (Pa)
R	Transient Bubble Radius = (mm)
R_0	Initial Bubble Radius (in Static Column) (mm)
R^2	Linear Correlation Coefficient
$P(t)$	Transient Pressure from Vibration (Pa)

Q_G	Gas Volumetric flux (lit/min)
r	Amplitude of Bubble Oscillation (mm)
Re	Reynolds Number
R_{air}	Specific Ideal Gas Constant (kJ/kg K)
T_G	Gas Phase Temperature
t	Time (s)
t_c	Contact (Residence) Time (s)
U_b	Bubble Terminal Velocity (m/s)
U_{SG}	Superficial Gas Velocity (mm/s)
V	Bubble Volume (mm ³)
V_0	Initial Bubble Volume (mm ³)
We	Weber Number

Subscripts

G	Gas
L	Liquid

Greek Symbols

ε	Void Fraction
ε_0	Void Fraction in static column
κ	Gas Heat Capacity
μ_L	Liquid Dynamic Viscosity (Pa s)
ν_L	Liquid Kinematic Viscosity (m s ⁻¹)
ρ_L	Liquid Density (kg m ⁻³)
ρ_G	Gas Density (kg m ⁻³)
σ	Gas-Liquid Surface Tension (N m ⁻¹)
σ_g	Geometrical Standard Deviation
τ	O ₂ Saturation Time Scale (s)
ϕ	Vibration Phase (Rad)
ω	Vibration angular velocity (Rad/s)

References

1. Harbaum, K.L.; Houghton, G. Effects of sonic vibrations on the rate of absorption of carbon dioxide in gas bubble-beds. *J. Chem. Technol. Biotechnol.* **1962**, *12*, 234–240. [[CrossRef](#)]
2. Houghton, G. The behaviour of particles in a sinusoidal velocity field. *Proc. R. Soc. Lond. A Math. Phys. Eng. Sci.* **1963**, *272*, 33–43. [[CrossRef](#)]
3. Jameson, G.J.; Davidson, J.F. The motion of a bubble in a vertically oscillating liquid: Theory for an inviscid liquid, and experimental results. *Chem. Eng. Sci.* **1966**, *21*, 29–34. [[CrossRef](#)]
4. Jameson, G.J. The motion of a bubble in a vertically oscillating viscous liquid. *Chem. Eng. Sci.* **1966**, *21*, 35–48. [[CrossRef](#)]
5. Houghton, G. Particle trajectories and terminal velocities in vertically oscillating fluids. *Can. J. Chem. Eng.* **1966**, *44*, 90–95. [[CrossRef](#)]
6. Rubin, E. Behavior of gas bubbles in vertically vibrating liquid columns. *Can. J. Chem. Eng.* **1968**, *46*, 145–149. [[CrossRef](#)]
7. Foster, J.M.; Botts, J.A.; Barbin, A.R.; Vachon, R.I. Bubble trajectories and equilibrium levels in vibrated liquid columns. *J. Basic Eng.* **1986**, *90*, 125–132. [[CrossRef](#)]
8. Marmur, A.; Rubin, E. Viscous effect on stagnation depth of bubbles in a vertically oscillating liquid column. *Can. J. Chem. Eng.* **1976**, *54*, 509–514. [[CrossRef](#)]
9. Tojo, K.; Nishimura, K.; Iwanaka, H.; Miyanami, K. Particle Movement in a Vertically Oscillating Liquid. *Bull. Univ. Osaka Prefect. Ser. A Eng. Nat. Sci.* **1981**, *30*, 41–53.
10. Baird, M.H.I.; Garstang, J.H. Gas absorption in a pulsed bubble column. *Chem. Eng. Sci.* **1972**, *27*, 823–833. [[CrossRef](#)]
11. Bretsznajder, S.; Jaszczak, M.; Pasiuk, W. Increasing the rate of certain industrial chemical processes by the use of vibration. *Ind. Chem. Eng.* **1963**, *3*, 496–502.

12. Krishna, R.; Ellenberger, J.; Urseanu, M.I.; Keil, F.J. Utilisation of bubble resonance phenomena to improve ga-liquid contact. *Naturwissenschaften* **2000**, *87*, 455–459. [[CrossRef](#)] [[PubMed](#)]
13. Krishna, R.; Ellenberger, J. Improving ga-liquid contacting in bubble columns by vibration excitement. *International journal of multiphase flow. Int. J. Multiph. Flow* **2002**, *28*, 1223–1234. [[CrossRef](#)]
14. Ellenberger, J.; Krishna, R. Shaken, not stirred, bubble column reactors: Enhancement of mass transfer by vibration excitement. *Chem. Eng. Sci.* **2003**, *58*, 705–710. [[CrossRef](#)]
15. Ellenberger, J.; Van Baten, J.M.; Krishna, R. Exploiting the Bjerknes force in bubble column reactors. *Chem. Eng. Sci.* **2005**, *60*, 5962–5970. [[CrossRef](#)]
16. Knopf, F.C.; Ma, J.; Rice, R.G.; Nikitopoulos, D. Pulsing to improve bubble column performance: I. Low gas rates. *AIChE J.* **2006**, *52*, 1103–1115. [[CrossRef](#)]
17. Knopf, F.C.; Waghmare, Y.; Ma, J.; Rice, R.G. Pulsing to improve bubble column performance: II. Jetting gas rates. *AIChE J.* **2006**, *52*, 1116–1126. [[CrossRef](#)]
18. Waghmare, Y.G.; Knopf, F.C.; Rice, R.G. The Bjerknes effect: Explaining pulsed-flow behavior in bubble columns. *AIChE J.* **2007**, *53*, 1678–1686. [[CrossRef](#)]
19. Waghmare, Y.G.; Rice, R.G.; Knopf, F.C. Mass transfer in a viscous bubble column with forced oscillations. *Ind. Eng. Chem. Res.* **2008**, *47*, 5386–5394. [[CrossRef](#)]
20. Waghmare, Y.G.; Dorao, C.A.; Jakobsen, H.A.; Knopf, F.C.; Rice, R.G. Bubble size distribution for a bubble column reactor undergoing forced oscillations. *Ind. Eng. Chem. Res.* **2009**, *48*, 1786–1796. [[CrossRef](#)]
21. Budzyński, P.; Dziubiński, M. Intensification of bubble column performance by introduction pulsation of liquid. *Chem. Eng. Proc. Process Intensif.* **2014**, *78*, 44–57. [[CrossRef](#)]
22. Budzyński, P.; Gwiazda, A.; Dziubiński, M. Intensification of mass transfer in a pulsed bubble column. *Chem. Eng. Proc. Process Intensif.* **2017**, *112*, 18–30. [[CrossRef](#)]
23. Gaddis, E.S. Mass transfer in ga-liquid contactors. *Chem. Eng. Proc. Process Intensif.* **1999**, *38*, 503–510. [[CrossRef](#)]
24. Mohagheghian, S.; Elbing, B.R. Characterization of Bubble Size Distributions within a Bubble Column. *Fluids* **2018**, *3*, 13. [[CrossRef](#)]
25. Hur, Y.G.; Yang, J.H.; Jung, H.; Park, S.B. Origin of regime transition to turbulent flow in bubble column: Orifice- and column-induced transitions. *Int. J. Multiph. Flow* **2013**, *50*, 89–97. [[CrossRef](#)]
26. Oliveira, M.S.N.; Ni, X. Gas hold-up and bubble diameters in a gassed oscillatory baffled column. *Chem. Eng. Sci.* **2001**, *56*, 6143–6148. [[CrossRef](#)]
27. Still, A.L.; Ghajar, A.J.; O'Hern, T.J. Effect of amplitude on mass transport, void fraction and bubble size in a vertically vibrating liquid-gas bubble column reactor. In Proceedings of the ASME 2013 Fluids Engineering Division Summer Meeting, Incline Village, NV, USA, 7–11 July 2013; p. V01CT17A004.
28. Elbing, B.R.; Still, A.L.; Ghajar, A.J. Review of bubble column reactors with vibration. *Ind. Eng. Chem. Res.* **2016**, *55*, 385–403. [[CrossRef](#)]
29. Besagni, G.; Inzoli, F.; Ziegenhein, T. Two-Phase Bubble Columns: A Comprehensive Review. *ChemEngineering* **2018**, *2*, 13. [[CrossRef](#)]
30. Simonnet, M.; Gentric, C.; Olmos, E.; Midoux, N. Experimental determination of the drag coefficient in a swarm of bubbles. *Chem. Eng. Sci.* **2007**, *62*, 858–866. [[CrossRef](#)]
31. Hinze, J.O. Fundamentals of the hydrodynamic mechanism of splitting in dispersion processes. *AIChE J.* **1955**, *1*, 289–295. [[CrossRef](#)]
32. Lewis, D.; Davidson, J.F. Bubble splitting in shear flow. *Trans. Inst. Chem. Eng.* **1982**, *60*, 283–291.
33. Wilkinson, P.M.; Spek, A.P.; van Dierendonck, L.L. Design parameters estimation for scale-up of high-pressure bubble columns. *AIChE J.* **1992**, *38*, 544–554. [[CrossRef](#)]
34. Gaddis, E.S.; Vogelpohl, A. Bubble formation in quiescent liquids under constant flow conditions. *Chem. Eng. Sci.* **1986**, *41*, 97–105. [[CrossRef](#)]
35. Besagni, G.; Inzoli, F. Novel gas holdup and regime transition correlation for two-phase bubble columns. In *Journal of Physics: Conference Series*; IOP Publishing: Bristol, UK, 2017.
36. Besagni, G.; Di Pasquali, A.; Gallazzini, L.; Gottardi, E.; Colombo, L.P.M.; Inzoli, F. The effect of aspect ratio in counter-current gas-liquid bubble columns: Experimental results and gas holdup correlations. *Int. J. Multiph. Flow* **2017**, *94*, 53–78. [[CrossRef](#)]
37. Clark, N.N.; Atkinson, C.M.; Flemmer, R.L.C. Turbulent circulation in bubble columns. *AIChE J.* **1987**, *33*, 515–518. [[CrossRef](#)]

38. Abràmoff, M.D.; Magalhães, P.J.; Ram, S.J. Image processing with ImageJ. *Biophotonics Int.* **2004**, *11*, 36–42.
39. Schneider, C.A.; Rasband, W.S.; Eliceiri, K.W. NIH Image to ImageJ: 25 years of image analysis. *Nat. Methods* **2012**, *9*, 671–675. [[CrossRef](#)] [[PubMed](#)]
40. Rasband, W.S. ImageJ. U.S. National Institutes of Health: Bethesda, MD, USA, 1997–2016. Available online: <http://imagej.nih.gov/ij> (accessed on 16 April 2013).
41. Besagni, G.; Inzoli, F.; Ziegenhein, T.; Lucas, D. Computational Fluid-Dynamic modeling of the pseudo-homogeneous flow regime in large-scale bubble columns. *Chem. Eng. Sci.* **2017**, *160*, 144–160. [[CrossRef](#)]
42. Guédon, G.R.; Besagni, G.; Inzoli, F. Prediction of ga-liquid flow in an annular gap bubble column using a bi-dispersed Eulerian model. *Chem. Eng. Sci.* **2017**, *161*, 138–150. [[CrossRef](#)]
43. Hedrick, T.L. Software techniques for two-and three-dimensional kinematic measurements of biological and biomimetic systems. *Bioinspiration Biomim.* **2008**, *3*, 034001. [[CrossRef](#)] [[PubMed](#)]
44. Xue, J.; Al-Dahhan, M.; Dudukovic, M.P.; Mudde, R.F. Bubble velocity, size, and interfacial area measurements in a bubble column by four-point optical probe. *AIChE J.* **2008**, *54*, 350–363. [[CrossRef](#)]
45. Xue, J.; Al-Dahhan, M.; Dudukovic, M.P.; Mudde, R.F. Four-point optical probe for measurement of bubble dynamics: Validation of the technique. *Flow Meas. Inst.* **2008**, *19*, 293–300. [[CrossRef](#)]
46. Miyauchi, T.; Oya, H. Longitudinal dispersion in pulsed perforated-plate columns. *AIChE J.* **1965**, *11*, 395–402. [[CrossRef](#)]
47. Bhaaga, D.; Weber, M.E. Bubbles in viscous liquids: Shapes, wakes and velocities. *J. Fluid Mech.* **1981**, *105*, 61–85. [[CrossRef](#)]
48. Brennen, C.E. *Fundamental of Multiphase Flow*, 1st ed.; Cambridge University Press: New York, NY, USA, 2005; pp. 60–66. ISBN 0521139988.
49. Majumder, S.K. *Hydrodynamics and Transport Processes of Inverse Bubbly Flow*; Elsevier: New York, NY, USA, 2016.
50. Hashimoto, H.; Sudo, S. Surface disintegration and bubble formation in vertically vibrated liquid column. *AIAA J.* **1980**, *18*, 442–449.
51. Hashimoto, H.; Sudo, S. Dynamic behavior of liquid free surface in a cylindrical container subjected to vertical vibration. *Bull. JSME* **1984**, *27*, 923–930. [[CrossRef](#)]



© 2018 by the authors. Licensee MDPI, Basel, Switzerland. This article is an open access article distributed under the terms and conditions of the Creative Commons Attribution (CC BY) license (<http://creativecommons.org/licenses/by/4.0/>).